A comprehensive Lagrangian flame–kernel model to predict ignition in SI engines

L. Cornolti, T. Lucchini, G. Montenegro and G. D'Errico*

Department of Energy, Politecnico di Milano, via Lambruschini 4, 20156 Milano, Italy

(*Received 19 October 2012; revised version received 3 May 2013; second revision received 18 July 2013; accepted 23 July 2013*)

1. Introduction

The initial formation and development of the flame kernel caused by spark discharge in internal combustion engines is a very complex phenomenon which has a non-negligible influence on the consequent combustion process. Different mechanisms interact and determine the success of the flame initiation and the initial expansion velocity. The high electrical potential difference across the spark-plug electrodes causes breakdown, creates a strong pressure wave and establishes a partially ionized plasma channel at high temperature [12,25]. Heat conduction and diffusion allow the kernel to expand before the combustion reactions take over and the combustion becomes self-sustainable [26]. Furthermore, different combustion regimes might be expected in the vicinity of the spark [1], depending not only on the engine load and speed, but also on the large variety of geometrical length scales existing in the combustion chamber (from 1 mm spark gap to several centimeters typical of the cylinder bore).

Because of its great influence on engine efficiency and cyclic variability, the initial flame development process in SI engines has been extensively studied over the years, to clarify

*Corresponding author. Email: gianluca.derrico@polimi.it

the relevant governing parameters and to provide general guidelines for numerical model development [7,11,16,28]. Recently, most of the efforts were focused on the improvement of multi-dimensional combustion models to include a realistic description of the first stages of the flame development process. In particular, suitable sub-models were developed to consider the energy transfer from electrical circuit to the gas phase, the initial thermal expansion of the ignited kernel at very high temperatures, the transition from thermal expansion to flame propagation and the effects of the local flow on the energy transfer. Hence to be eligible for a possible implementation into a computational fluid dynamics (CFD) code, a numerical model should give a positive answer to the following questions:

- Is the electrical circuit modelled?
- Is the initial kernel modelled?
- Are high- and low-temperature effects taken into account in the kernel expansion?
- Are the local mixture and flow-field conditions considered?
- Is there a strict coupling between the flame kernel and the CFD models?
- Are possible re-ignition considered?
- Was the model validated with experimental data?

Due to the high requirements in terms of mesh resolution associated with the use of Eulerian models [25], Lagrangian models are generally employed: a set of particles is placed in the vicinity of the spark plug, each of them representing a part of the ignited kernel and evolves in time. Starting from this idea, models with different levels of detail have been proposed: the *DPIK* model (Discrete Particle Ignition Kernel) [24] and its modifications [10], the *AKTIM* (Arc and Kernel Tracking Ignition Model) model proposed by Duclos and Colin [8] and the more recent *Spark-CIMM* model introduced to predict combustion in stratified-charge, direct-injection engines, where mixture distribution, flow field and turbulence play a very important role in the development of the combustion process [6]. Recently, the possibility to massively parallelize CFD computations and to use techniques such as Adaptive Local Mesh Refinement [14] allowed the application of Eulerian ignition models also to engine simulations. An example of them is the so-called *Spark Energy Deposition Model* that was applied in [27] to simulate a stratified-charge, direct-injection engine. A well-mixed model, based on detailed chemistry, was used for combustion with the mixture ignited by the heat transferred from the electrical circuit. To account for local flow conditions, the heat transfer source was convected from the centre of the spark plug by the gas flow.

At this point, it should be pointed out that already available approaches are mainly focused on several aspects of the ignition process but none of them accounts for all the phenomena. For example, DPIK-derived models are very detailed in the computation of flame surface density and initial thermal expansion of the ignited volume, but effects of local flow and air–fuel ratio distribution are almost neglected. On the other hand, AKTIM and Spark-CIMM describe very carefully how initial flame development is affected by flow and turbulence, but effects of energy transfer on flame kernel growth are taken into account in a simplified way. In this work, the authors intend to present a comprehensive multi-dimensional model of the combustion process in spark-ignition engines and show a preliminary validation.

To fulfil the proposed requirements, the most advanced aspects of the available literature models have been combined. In particular, the spark channel is initially represented by a set of lagrangian particles, which are initially placed along the spark gap [5]. Particles are convected by the mean flow and, for all of them, equations of mass and energy are solved. Specific sub-models estimate the instantaneous amount of energy transferred from the electrical circuit to the kernels and calculate the flame expansion velocity accordingly, taking into account the real properties of the high-temperature gas [4]. At each time step, the flame surface density distribution is reconstructed once

particle positions and their radius are known [10]. Such quantity is then used by the combustion model to calculate the fuel burning rate.

The proposed set of models has been implemented into the Lib-ICE code, which is a set of libraries and solvers for the simulation of IC engines developed under the OpenFOAM® technology [19]. Examples of application of Lib-ICE to the simulation of real engine operation including gas exchange, fuel–air mixing and combustion are provided in [3,15,17]. Preliminary experimental validation was carried out through the database by Herweg *et al.* [16] and Maly and Herweg [11]. It consists of a set of well-documented experiments of spark-ignition combustion carried out in an optical, pre-chamber engine. The choice of such a database was mainly justified by the fact that a very wide range of operating conditions was analysed. Variation of engine speed, air–fuel ratio and spark-plug position makes possible to test the model under different combustion regimes. Furthermore, since two different ignition systems were used in the experiments, sensitivity of the model with respect to the electrical circuit can be also evaluated. For any tested operating condition, computed and experimental data of burned gas volume are compared.

The rest of the paper will be organized as follows. First, the multi-dimensional model will be described, then a short assessment of the model behaviour will be shown. Finally, the experimental set-up proposed in [11,16] will be described and its results will be used to preliminarily validate the model.

2. Numerical models

The proposed approach to describe the flame kernel development process in spark-ignition engines consists of a set of different sub-models interacting among each others and exchanging information with the CFD code. A schematic of the model implementation is provided in Figures 1 and 2. When spark discharge takes place, the ignited channel is represented by a set of Lagrangian particles that are placed along the spark-gap distance. These particles are used to track the spark evolution, but they also represent the centre of spherical kernels whose envelopment defines the flame surface. Suitable correlations can be used to estimate the diameter and temperature of the spark channel immediately after breakdown. Before the tracking algorithm is performed, computed flow-field data such as ambient density, turbulence quantities (k and ε), laminar flame speed and velocity field are passed to the ignition model. Particles are convected by the mean flow and they grow in size because of flame speed (s_T) and thermal expansion (s_{plasma}) due to the heat transferred from electrical circuit to the gas phase ($\dot{Q}_{spk}$). Such quantity is provided by a suitable model that predicts the current and voltage evolution inside the secondary circuit. Once particle tracking is performed, the flame surface density field (Σ) is reconstructed and passed to the transport equation of the ECFM (extended coherent flamelet model) combustion model [2,9]. In the next sections, the following required sub-models will be described more in detail:

- Particle evolution model (initialization, tracking, mass and energy equations).
- Plasma channel model.
- Electrical circuit model.
- Flame surface density calculation.

2.1 *Particle evolution model*

The breakdown is a strong non-equilibrium thermodynamic process which lasts for few nanoseconds, therefore it is not modelled. The initial temperature and diameter of the particles are set with the presumed value assumed after breakdown using the equations suggested in the work by Song

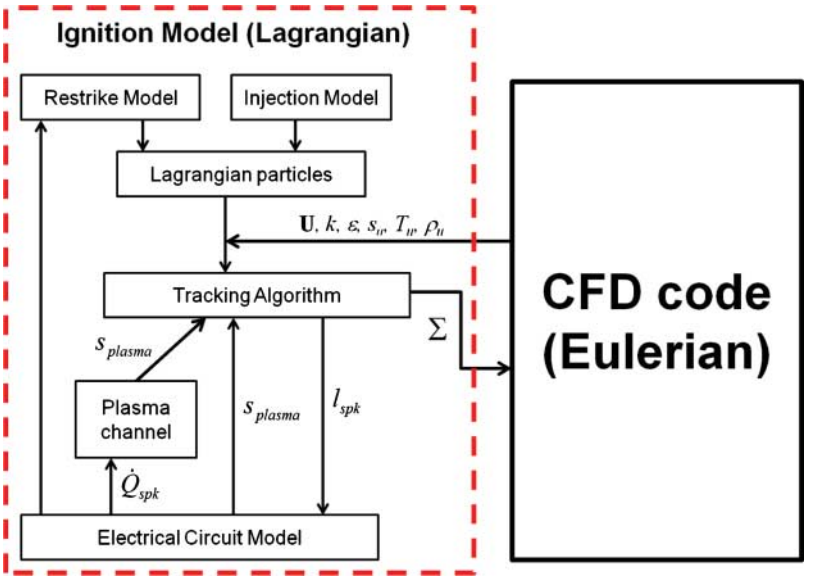

Figure 1. Schematic of the Lagrangian ignition model implemented in this work: model-to-model interaction and exchange of information with the CFD code.

and Sunwoo [23]. The temperatures obtained are of the order of 40,000 K and make the initial thermal expansion not negligible. Once particles are introduced in the computational mesh, they are convected by the mean flow, with their position changing as follows:

$$\frac{\mathrm{d}\mathbf{x}_\mathrm{p}}{\mathrm{d}t} = \mathbf{U}_\mathrm{g}, \tag{1}$$

where $\mathbf{U}_\mathrm{g}$ is the gas velocity at particle position, which is interpolated by means of the so-called *cell-point-face* technique [18], which ensures a continuous gas velocity field for each particle along its trajectory with a reduced dependency of the computed results from the grid size. Lagrangian particles represent possible locations of a ignited kernel. For each of the kernels, mass and energy conservation equations are solved. Both mass conservation and radius variation equations account for contributions due to thermal expansion and turbulent flame speed:

$$\frac{\mathrm{d}m_\mathrm{p}}{\mathrm{d}t} = 4\pi \cdot r_\mathrm{p}^2 \cdot \rho_\mathrm{u} \cdot \left(s_\mathrm{T} + \frac{\rho_\mathrm{k}}{\rho_\mathrm{u}} s_\mathrm{plasma} \right), \tag{2}$$

$$\frac{\mathrm{d}r_\mathrm{p}}{\mathrm{d}t} = \frac{\rho_\mathrm{u}}{\rho_b} s_\mathrm{T} + s_\mathrm{plasma}, \tag{3}$$

with r_p being the particle radius and ρ_u the unburned gas density at particle position. s_T is the turbulent flame speed, which is computed from laminar flame speed s_u at particle position and flame wrinkling Ξ:

$$s_\mathrm{T} = \Xi \cdot s_\mathrm{u}, \tag{4}$$

$$\frac{\mathrm{d}\Xi}{\mathrm{d}t} = P \cdot \Xi - D_\mathrm{k}, \tag{5}$$

with P and D_k being the production and destruction terms commonly used in the ECFM combustion model. Their formulation can be found in [9,10]. To compute the second RSH term in Equation (2), representing the flame kernel expansion velocity due to energy transfer from the

electrical circuit, it is necessary to distinguish between the two different mechanisms governing flame kernel growth:

(1) Heat conduction from the hot plasma channel to the unburnt mixture. In such a condition, temperature distribution inside the flame kernel is not uniform.
(2) Expansion due to chemical reactions and heat transfer from the electrical circuit. Temperature is uniform inside the flame kernel and composition is at chemical equilibrium.

At the beginning of the spark-discharge process, when flame kernel temperature is much higher than a threshold value, a specific sub-model (plasma channel model) predicts the heat conduction inside the channel and computes s_{plasma} and the other properties of each kernel (temperature, density and radius) accordingly. At lower temperatures, when the flame kernel expansion is mainly governed by chemical reactions, the temperature T_{p} inside the flame kernel can be considered uniform and is computed through the following energy conservation equation:

$$\frac{\mathrm{d}T_{\text{p}}}{\mathrm{d}t} = -\frac{m_{\text{p}}}{\dot{m}_{\text{p}}}(T_{\text{p}} - T_{\text{b}}) + \frac{\dot{Q}_{\text{spk}} \cdot \eta_{\text{eff}}}{m_{\text{p}} c_{\text{p}}} + \frac{1}{\rho_{\text{b}} c_{\text{p}}} \cdot \frac{\mathrm{d}p}{\mathrm{d}t}, \tag{6}$$

with ρ_{b} being the burned gas density and T_{b} the adiabatic flame temperature. While s_{plasma} is computed according to [5,24]:

$$s_{\text{plasma}} = \frac{\dot{Q}_{\text{spk}} \cdot \eta_{\text{eff}}}{4 \cdot r_k^2 \cdot (u_{\text{k}} - h_{\text{u}}) + p(\rho_{\text{u}}/\rho_{\text{k}})}, \tag{7}$$

where $\dot{Q}_{\text{spk}}$ is the energy transferred from the electrical circuit whose computation is explained in the electrical circuit model section, η_{eff} is the efficiency of the energy transfer [16], h_{u} is the specific enthalpy of the flame kernel, u_{k} and ρ_{k} are the kernel specific enthalpy and density, respectively. The temperature threshold used to switch from one regime to the other is, as suggested by Falfari and Bianchi [10] and Shen *et al.* [22], three times the adiabatic flame temperature.

2.2 *Plasma channel model*

When $T_{\text{p}} > 3T_{\text{ad}}$ heat conduction effects cannot be neglected in the gas surrounding the ignited kernel. For this reason, temperature distribution and its effects on s_{plasma} need to be modelled in detail. Until temperature remains higher than $3T_{\text{ad}}$, all the flame kernels related to the same discharge event are assumed to have the same temperature distribution, which is computed by solving the heat conduction equation for the space-dependent plasma temperature T_{pl}:

$$\frac{\partial T_{\text{pl}}}{\partial t} = \nabla \cdot (\alpha \cdot \nabla T_{\text{pl}}) + \frac{\eta_{\text{eff}} \cdot \dot{Q}_{\text{spk}}}{\rho_{\text{pl}} \cdot c_{\text{p,pl}} \cdot V_{\text{pl}}}, \tag{8}$$

where α is the plasma thermal diffusivity. A sub-cycling procedure ($\Delta t = 20$ ns) is used to solve Equation (8), which is discretized on a 1D, axy-symmetric grid representing a sector of the gas region that surrounds the spark electrodes. The mesh height is set to be equal to d_{gap}, while the radial length of the domain is set to 1 cm, which is significantly higher than the maximum diameter of the flame kernel that is reached during this phase. The grid size is 10 μm and the following initial and boundary conditions were imposed at spark time and after each restrike event:

$$t = t_0 : \; T_{\text{pl}} = T_i \quad \text{if } 0 < r < r_i, \quad T_{\text{pl}} = T_{\text{unb}} \quad \text{if } r < r_i,$$
$$r = r_\infty : \; T_{\text{pl}} = T_{\text{unb}},$$

where T_i and r_i are, respectively, the temperature and radius after the breakdown. Following Maly and Herweg [16], at each time step the flame kernel radius r_{k} is identified as the location where

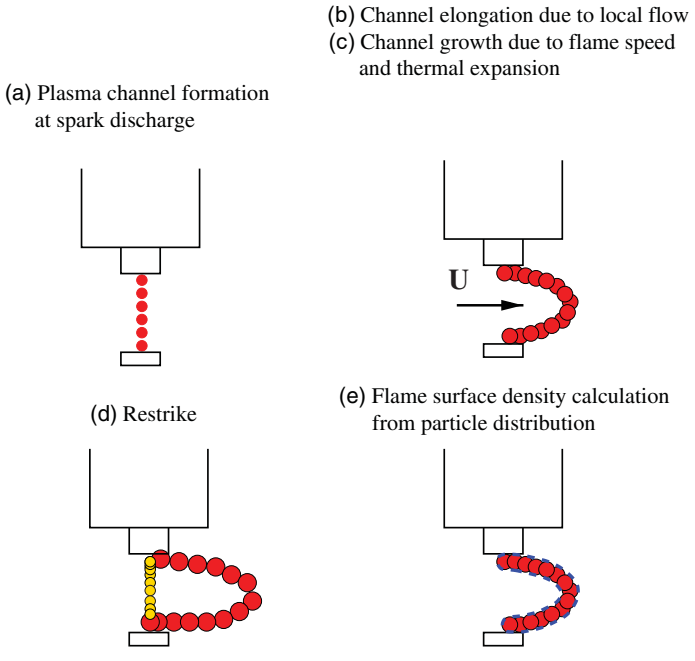

Figure 2. Details of the ignition model implemented in this work (a–b–c): creation and evolution of the spark channel; (d) formation of multiple channels due to the restrike phenomenon and (e) coupling with the CFD code through the calculation of the flame surface density distribution.

the adiabatic flame temperature is found in the spark-channel 1D mesh. In this way, the expansion velocity s_{plasma} can be computed as follows:

$$s_{\text{plasma}} = \frac{r_{\text{k}}(t + \Delta t_{\text{CFD}}) - r_{\text{k}}(t)}{\Delta t_{\text{CFD}}}. \tag{9}$$

To properly solve Equation (8), temperature dependency of the plasma properties such as thermal diffusivity α_{pl}, heat capacity $c_{\text{p,pl}}$ and density ρ_{pl} need to be known. These effects were taken into account by assuming thermodynamic and chemical equilibrium and neglecting fuel contribution. In this way, it was possible to employ the thermodynamic and transport properties functions provided in [4]. In their work D'Angola *et al*. computed the composition, thermodynamics and transport properties of equilibrium air plasmas in a wide range of pressures and temperatures (0.01–100 atm and 50–60,000 K). Then they interpolated the results with a single complex function for each property and provided the coefficients.

Figure 3 provides an example of temperature dependency for plasma thermal diffusivity. The oscillations are mainly related to the changes in chemical composition which is due to the ionization and dissociation processes at high temperatures. It should be remarked that thermal diffusivity significantly increases with temperature so that the effect of thermal expansion is not only influenced by temperature gradient but also by gas properties.

2.3 *Electrical circuit model*

The way energy is transferred from the electrical circuit to the gas phase might affect significantly the flame kernel development process, mainly in presence of lean mixtures (low s_{u}), high ratio between turbulence and laminar flame speed (u'/s_{u}), or high gas flow velocities, for this reason also a model of the electrical circuit has been implemented. Usually, SI engines employ transistor-controlled ignition (TCI) ignition systems, basically composed of a primary and a secondary circuit coupled by a transformer, which, neglecting parasitic impendence and inductance, can be

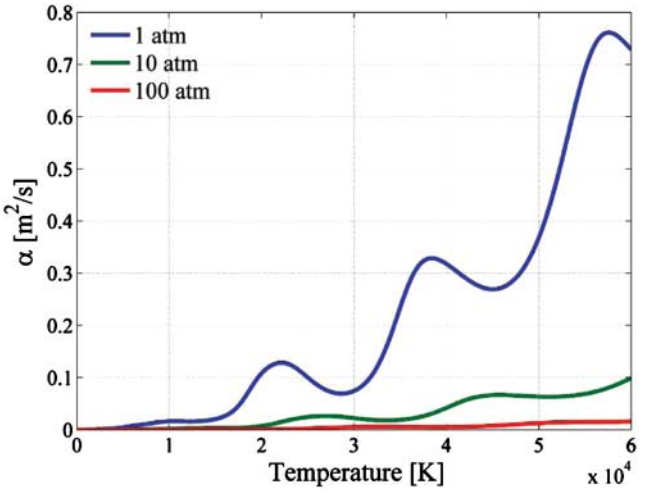

Figure 3. Temperature dependency of $\alpha_{p,pl}$ in the 50–60,000 temperature range at different ambient pressures.

schematically illustrated as in Figure 4. After the spark-time, the primary switch is opened and the voltage across the electrode rapidly reaches the breakdown value. After that, the primary circuit influence on the following evolution of the current profile is negligible and the energy equation of the circuit can be reduced to

$$\frac{dE_s}{dt} = -R_s i_s(t) - V_{ie} i_s(t), \tag{10}$$

$$E_s = \tfrac{1}{2} L_s i_s^2, \tag{11}$$

where E_s is the energy stored during the charge time reduced by the breakdown energy computed as in [10], R_s is the equivalent resistance of the secondary circuit, L_s the secondary circuit inductance and V_{ie} is the inter-electrode voltage fall, computed as the sum of three terms: voltage in the gas column, cathode and anode voltage falls [13]. The values of L_s and R_s have to be tuned with experimental data of spark discharge at quiescent conditions. For more complex behaviour of the plasma channel (discharge with dilated transition from arc phase to glow phase) or different ignition systems, experimental voltage and current profile have to be imposed. Once the current is known, the energy release to the gas phase is computed as follows:

$$\dot{Q}_{spk}(t) = V_{gc}(t) \cdot i_s(t), \tag{12}$$

where V_{gc} is only the gas column voltage because the anode and cathode voltage fall affects a very thin region of few mean free paths [20]. Equation (6) requires also an additional parameter representing the efficiency of the energy transfer process η_{eff}. Experiments from Maly and Herweg [16] illustrate that the flow field in the vicinity of the spark plug significantly affects η_{eff} during both arc and glow discharge processes. In particular, when the discharge channel is elongated by the flow field, the ratio of the column voltage V_{gc} to the anode and cathode fall increases and the heat losses to the electrodes decrease. Hence, the correlation proposed in [16] was employed in the present work. Moreover, experimental observations [13] show that when the voltage fall across the electrodes becomes greater than a threshold value, the plasma channel moves back to the original inter-electrode space. Such a process is called *restrike* and can influence the combustion process especially when the discharge lasts for a long time and the flow between the electrodes is characterized by a consistent mean velocity. Restrike is assumed to take place every time the gas column voltage becomes higher than a threshold value. In the proposed approach, when restrike

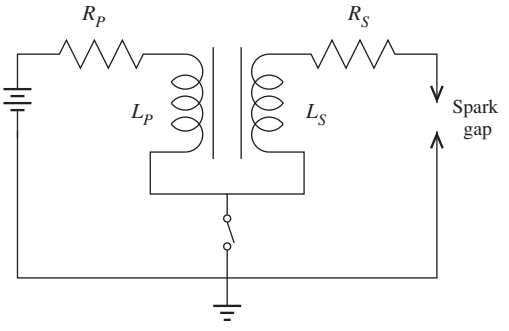

Figure 4. Simple schematic of the TCI ignition system.

occurs, a new set of particles is placed along the spark gap. The old particles continue to evolve inside the computational domain, but they lose the corresponding heat term in the energy equation.

2.4 *Flame surface density calculation*

Once the particles are tracked in the computational mesh, it is necessary to reconstruct the flame surface density distribution resulting from particle size and positions. This operation is performed in several steps:

(1) A spherical triangulated surface is placed at any particle location.
(2) The radius of each sphere is adjusted to match the value of the representative particle.
(3) The flame surface is defined by the total amount of non-intersecting triangles of the placed spheres.
(4) The number of triangular faces N_f belonging to each computational cell is identified.
(5) For any cell, the flame surface density Σ is computed as follows:

$$\Sigma_\mathrm{k} = \frac{(\sum_{i=1}^{N_\mathrm{f}} S_i)}{V_\mathrm{cell}}, \tag{13}$$

where S_i is the area of each triangle. An insight about how flame surface density is computed is provided in Figure 2(e). Distribution of Σ_k is then used to estimate the reaction rate source term in the progress variable equation, according to the flame surface density formulation. When one of the kernels radius reaches a threshold value (in our calculations this value was set to 2 mm as in [10]), the combustion model switches to a complete Eulerian description and both the progress variable and the Σ equations are solved. The Σ field is initialized with the profile provided by the method previously described. The coupling between Eulerian gas phase and Lagrangian ignition model is only done through the flame surface density distribution, while energy from the electrical circuit is not transferred to the ambient gas, but only to the Lagrangian particles. This choice was mainly motivated by the complexity that is required to compute chemical equilibrium and gas properties in the 5000–50,000 K range, accounting for proper species composition in the burned gases.

3. Ignition model assessment

In order to assess the model behaviour, the development of a single channel was analysed at different operating conditions. Figures 5 and 6 illustrate computed evolutions of channel diameter and temperature for the 300 rpm case with central ignition location. Consistent with the literature, the

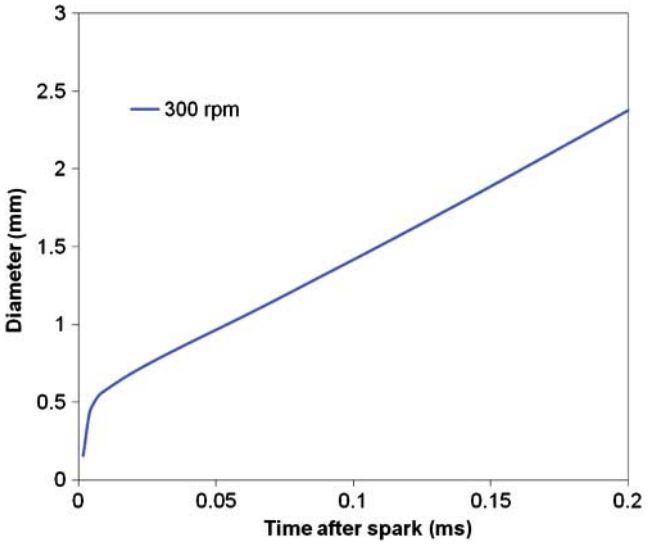

Figure 5. Single channel diameter evolution of for the 300 rpm case with central ignition.

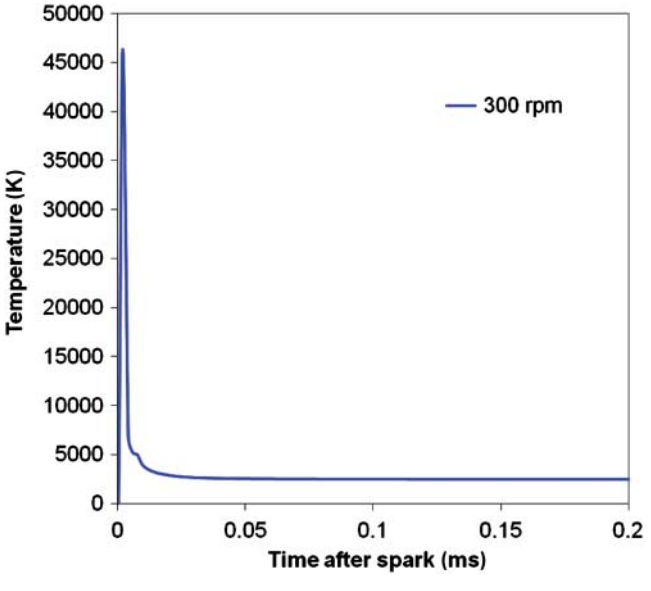

Figure 6. Single channel temperature evolution of for the 300 rpm case with central ignition.

model predicts that initially ($t < 10$ ns) the channel diameter rapidly grows due to heat conduction inside the plasma channel, later ($t > 50$ ns) the same process is mainly governed by flame propagation and heat transfer from the electrical circuit. For what concerns the temperature evolution, initially the channel is very hot ($T \sim 45{,}000$ K), then its temperature is fast reduced due to heat conduction. When flame propagation and heat conduction are the relevant phenomena, channel temperature stabilizes at values that are slightly higher than the adiabatic flame temperature.

The model can correctly reproduce the effects of turbulence on flame kernel growth. In particular, Figure 7 shows the computed channel expansion velocity for two different engine speeds: 300 and 1250 rpm. Initially, thermal expansion dominates and velocity is very high. After a minimum value is reached approximately at 30 ns, velocity grows due to the establishment of a turbulent

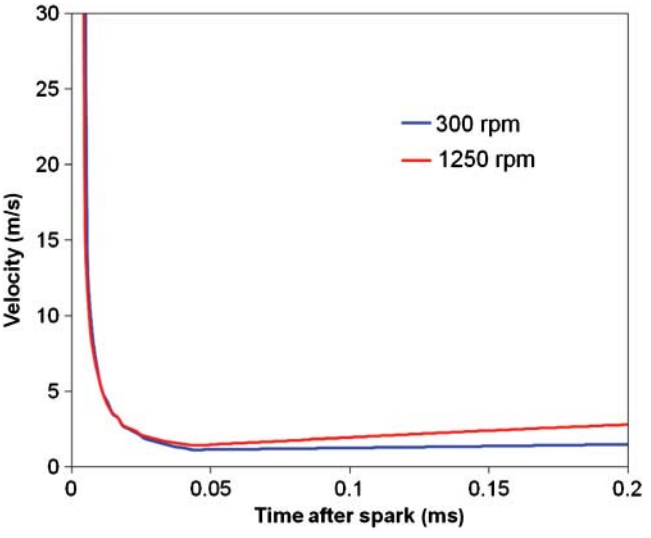

Figure 7. Comparison between computed flame kernel growth velocities for the 300 and 1250 rpm cases with central ignition.

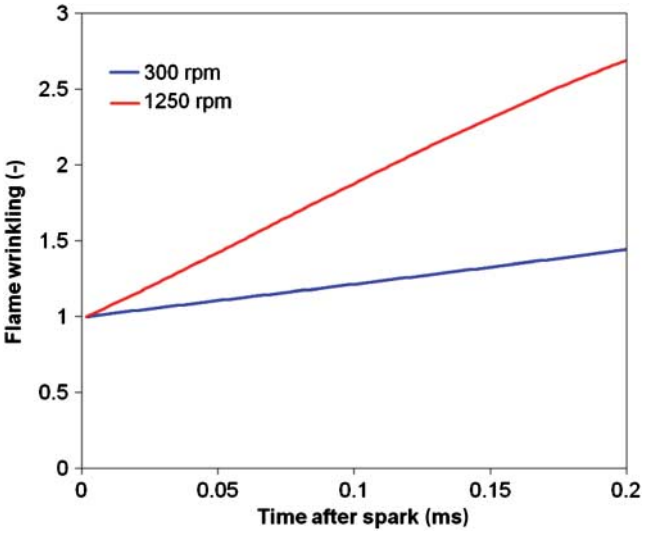

Figure 8. Computed evolution of the flame wrinkling factor for a single channel at 300 and 1250 rpm.

flame, with a higher wrinkling for the 1250 rpm case. This observation is confirmed in Figure 8, which displays the evolution of the flame wrinkling factor for the two conditions. In the 1250 rpm case, turbulence plays an important role even in the initial flame kernel development. Effects of relative air/fuel ratio are summarized in Figure 9 for the cases with central ignition at 1250 rpm, where it is possible to see how, after the initial predominant thermal expansion, the flame kernel growth is significantly affected by mixture conditions, with the expansion velocity for the lean cases being significantly lower than the stoichiometric one due to the dependency of the laminar flame speed on the air/fuel ratio.

So far, the behaviour of the proposed model can be considered rather satisfactory. Effects of local flow, air/fuel ratio and turbulence are correctly represented. For this reason, it will be possible to perform a preliminary validation with experimental data.

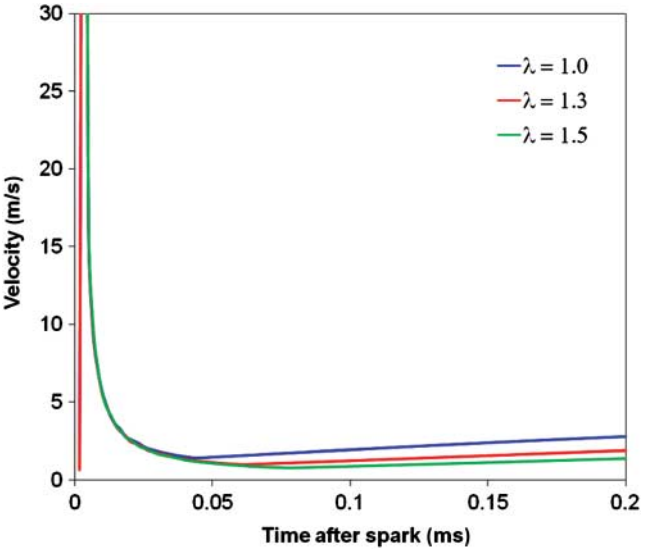

Figure 9. Effects of relative air/fuel ratio on single channel grow velocity.

4. Experimental comparison

4.1 *Test case set-up and flow prediction*

In this study, the experiments from Maly and Herweg [16] are used for the comparison with the model results. The test engine was designed to induce a strong swirl motion inside a side chamber (Figure 10) where combustion occurs. By varying the engine speed and the spark position, i.e. in the centre of the chamber and at a peripheral zone, Herveg and Maly investigated separately the effects of mean flow velocity and turbulence intensity on the development of the flame kernel. Thanks to optical access provided by two large quartz windows at both cylinder ends and two circumferential windows, Laser Doppler velocimetry (LDV) measurement of velocities and turbulence intensity at the peripheral spark position and high-speed Schlieren filming were allowed. From the images of the flame taken from the two pair of orthogonal windows, Herweg *et al.* estimated the burned volume at different crank angles. The experimental data provided in [16] cover 60 operating conditions including a wide range of engine speeds (300, 500, 750, 1000 and

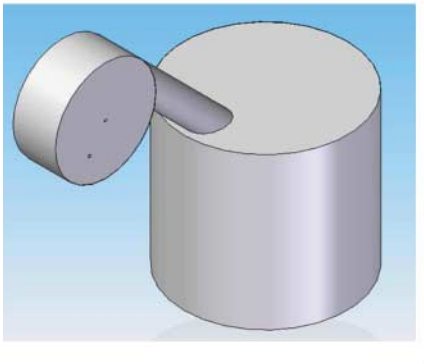

	Ignition system	Engine speed [rpm]	Air index λ [-]	Spark location
CASE 1	TCI	300	1	CENTRAL
CASE 2	TCI	750	1	CENTRAL
CASE 3	TCI	1250	1	CENTRAL
CASE 4	TCI	1250	1.3	CENTRAL
CASE 5	TCI	1250	1.5	CENTRAL
CASE 6	TCI	300	1	PERIPHERAL
CASE 7	TCI	750	1	PERIPHERAL
CASE 8	TCI	1250	1	PERIPHERAL
CASE 9	TCI	1250	1.3	PERIPHERAL
CASE 10	TCI	1250	1.5	PERIPHERAL

Figure 10. CAD of the cylindrical transparent side engine chamber and list of the simulated operating conditions.

1250 rpm), several stoichiometries (air index: 1.0, 1.3 and 1.5), two different spark-plug positions (central and peripheral) and finally two different ignition systems (TCI and CDI (capacitor discharge ignition)). In this work, 10 representative cases were considered. In particular, because of the applied electrical circuit model, only the TCI system was considered. The list of the tested cases can be found in the table of Figure 10. To correctly predict the velocity field inside the side chamber, the compression phase from inlet valve closure to ignition time was computed. The initial gas temperature was set to 293 K according to the experimental data, cylinder walls were considered adiabatic and, for any operating condition the initial cylinder pressure was adjusted to reach the experimental value of 0.5 MPa measured at ignition time. Quiescent conditions were initially assumed in the entire cylinder, and the turbulence model used was the standard k–ϵ. The geometry of the connecting duct was simplified to get a good-quality hexahedral mesh which allowed the use of second-order methods for all the computed quantities. To be able to represent the flow near the electrodes, a fine mesh of about 0.15 mm was necessary. Figure 11(a) illustrates the used CFD mesh, which consists of about 250,000 cells.

Figure 11(b) shows the velocity field at ignition time. The jet from the cylinder, at this stage, is definitely tangential to the side chamber and the strong swirl motion produced is not completely

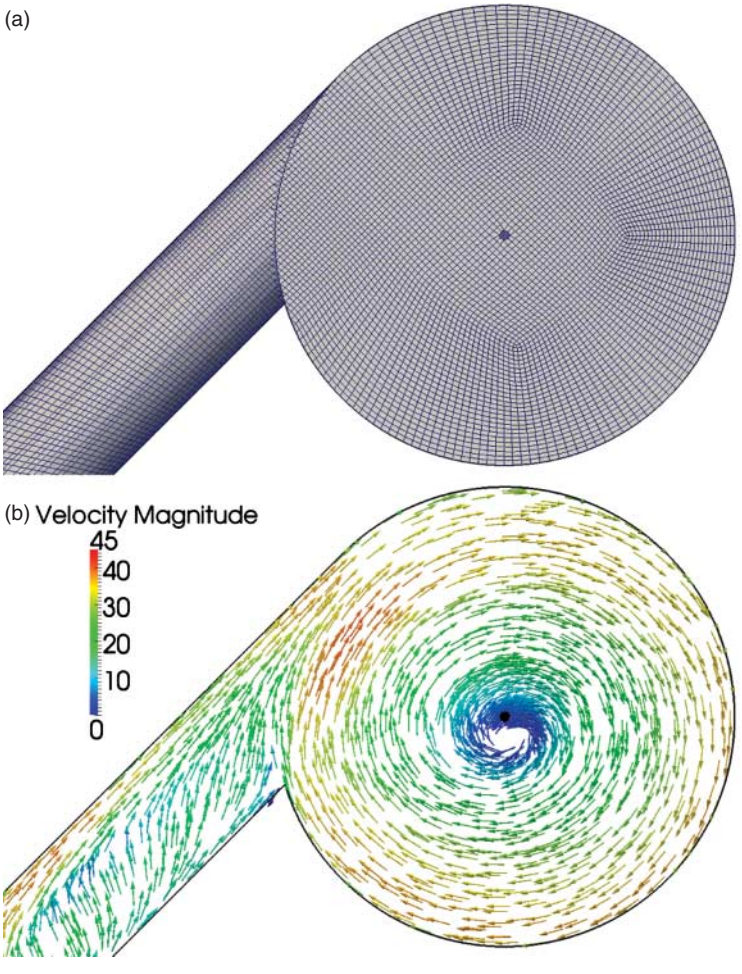

Figure 11. CFD mesh of the side engine chamber (a) and computed velocity field at ignition time (b).

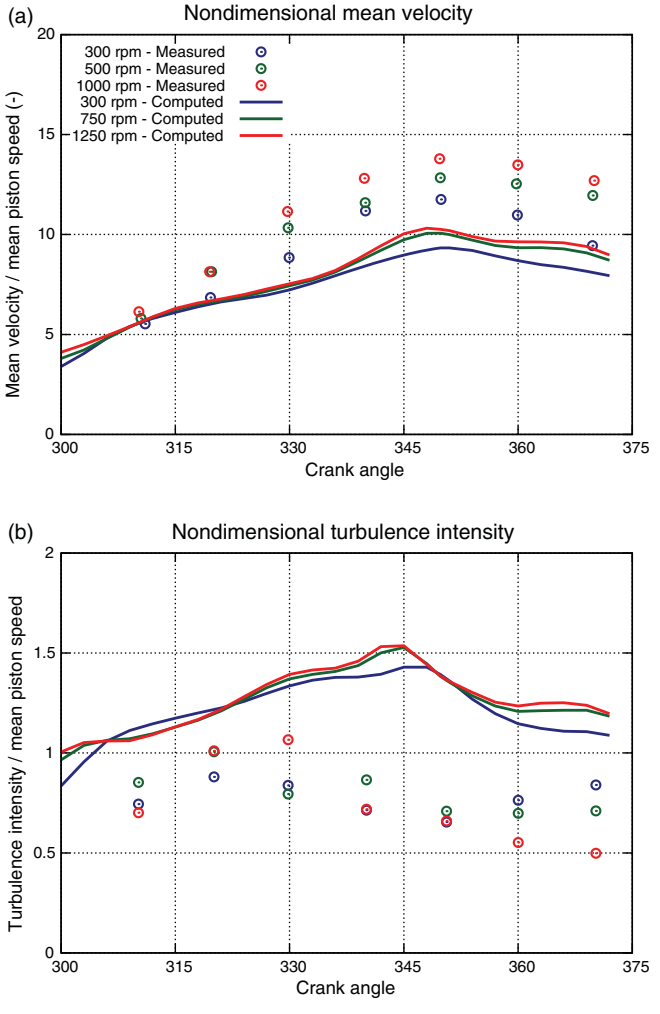

Figure 12. Computed and measured [11] average velocity (a) and turbulence intensity (b) at the peripheral spark position.

centred so that a low but not negligible mean velocity is found at the central spark plug. The comparison of computed and experimental average velocity and turbulence intensity at the peripheral spark position (Figure 12) shows that the computed velocity is a bit lower than the experimental one, while the turbulence intensity is overestimated. However, considering the existing uncertainties about the initial condition, how the charge process is accomplished and the position of the LDV measurement, we considered the results acceptable for our purposes.

Figure 13 shows the computed velocity and turbulence intensity profile along the radius of the chamber passing through the centre and the peripheral spark position. It can be seen that the minimum velocity is found at about 10% of the chamber radius and that while the velocity changes significantly with the distance from the centre, the turbulence level is more uniform.

4.2 *Comparison between ignition model and experimental data*

Once the CFD model has been assessed in terms of predicted velocity and turbulence intensity at the spark location, it was applied to determine the flame kernel evolution for the different

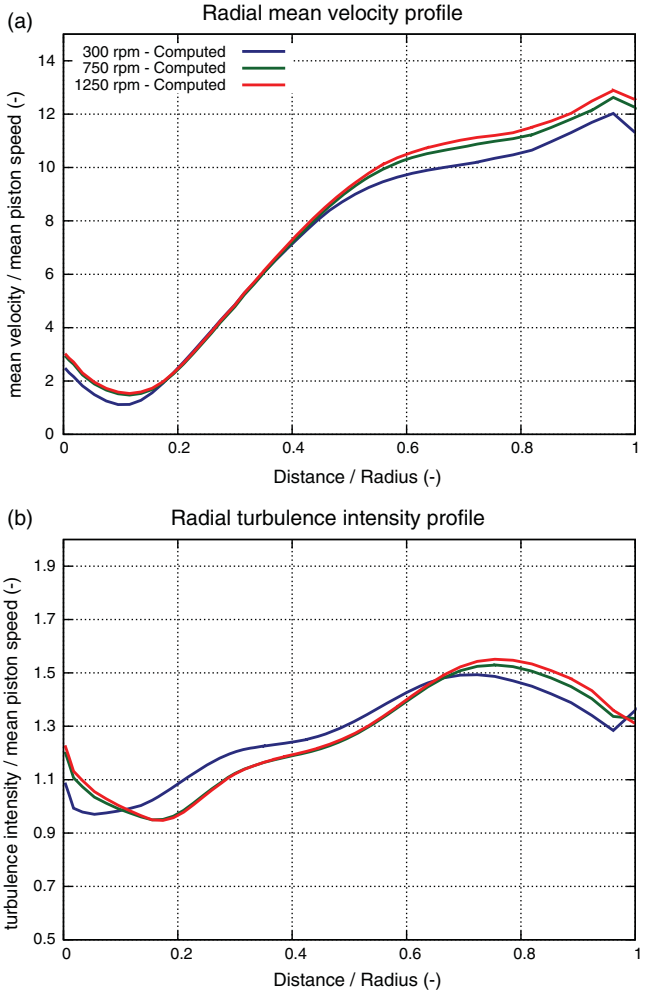

Figure 13. Computed average velocity (a) and turbulence intensity (b) along the radius of the chamber passing through the centre and the peripheral spark position.

operating conditions which were selected. In order to have a quantitative assessment of the model capabilities, the measured and computed time taken from the flame kernel to reach a defined burnt volume is compared. In [16] the minimum volume for which these data are reported is 0.1 cm^3, so this value was taken as reference. It can be observed that we can assume the flame kernel growth to be dominated by the properties of the ignition system as long as its radius is less than 1 mm. Since a volume of 0.1 cm^3 corresponds to a sphere with a radius of about 3 mm, the time taken by the flame to define such a volume is significantly influenced by the properties of the ignition system, but also laminar and in minimum part turbulent flame properties have a non-negligible effect. In the post-processing of the CFD results, the burnt volume was obtained on the basis of the gas density, the progress variable and the volume in each cell of the domain:

$$V_{\mathrm{b}} = \sum_{i=1}^{n} \frac{\rho_i V_i c_i}{\rho_{\mathrm{b},i}}, \tag{14}$$

where the subscript b refers to the burnt gas.

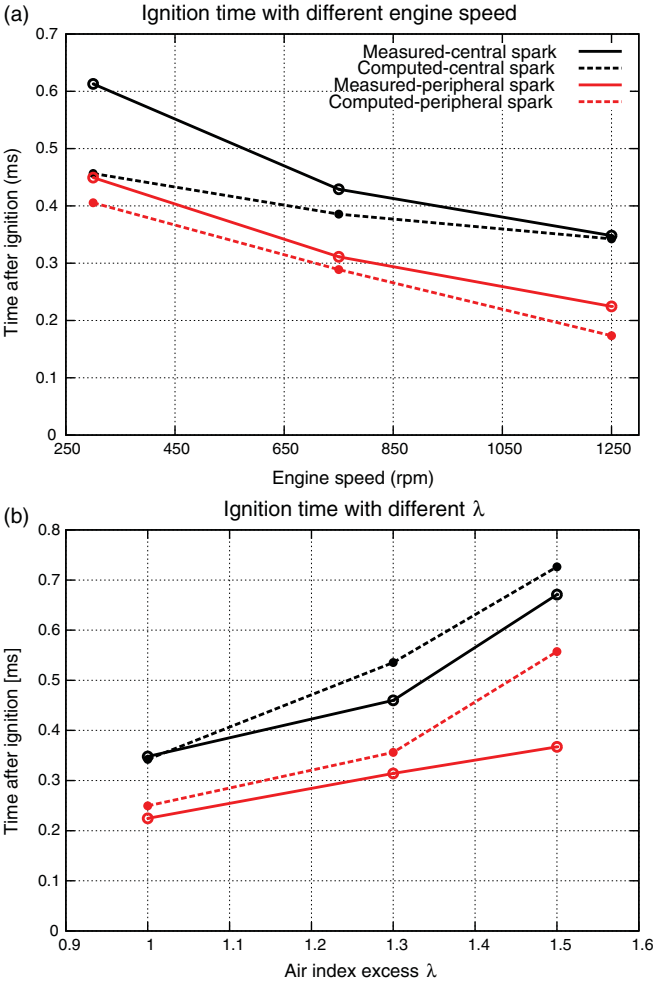

Figure 14. Measured and computed time taken from the flame kernel to reach a volume equal to 0.1 cm^3 at $\lambda = 1$ as a function of the engine speed (a) and at 1250 rpm as function of the air-index excess (b).

In Figure 14(a), the measured and computed time taken by the flame kernel to reach the volume of 0.1 cm^3 at stoichiometric conditions for three engine speeds and for both spark locations is shown. The model captures rather well the reduction of the time taken by the flame kernel for the configuration with the peripheral location with respect to the corresponding value with the central ignition. This difference is mainly due to the effects of the velocity, which supports the kernel growth by convecting the kernel out of the electrode region and enhances the energy transfer to the gas, and of the turbulence intensity, which is higher in the proximity of the peripheral location. The model also reproduces the increase in flame velocity with the engine speed which is due to the increase in turbulence intensity inside the combustion chamber as shown in Figure 11, whose graphs are normalized with respect to the mean piston speed. The main difference between measured and computed data which was found is regarding the underestimation of the increase in time at 300 rpm in the case of central ignition. This issue needs further investigation, especially since the comparison between measured and computed data is rather good for the same engine speed and the peripheral ignition, with initial conditions which are similar under this condition since the engine speed is very low. Figure 14(b) shows the same comparison between the measured

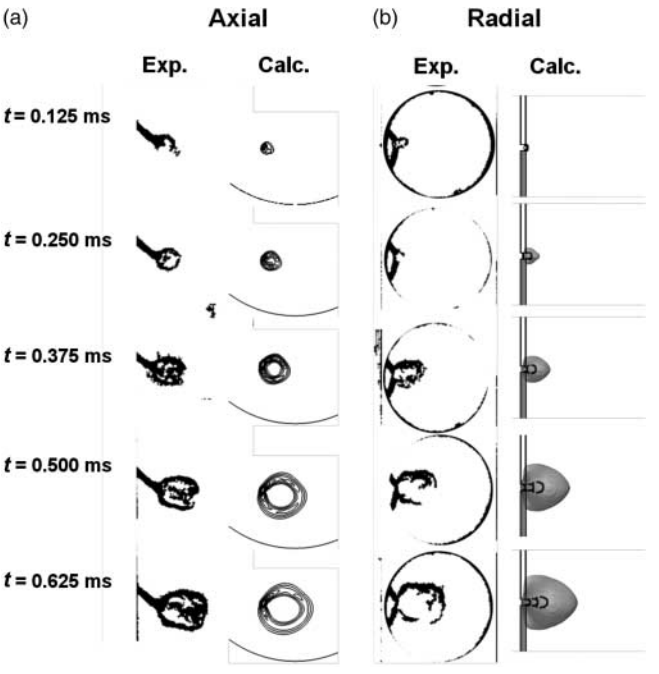

Figure 15. Comparison between experimental Schlieren images and computed contours of density gradient magnitude [21]. (a) Axial view. (b) Radial view with computed contours of progress variable taken at $c = 0.5$, location of channel particles represented with black points. Engine speed: 300 rpm, lambda 1.0, peripheral ignition.

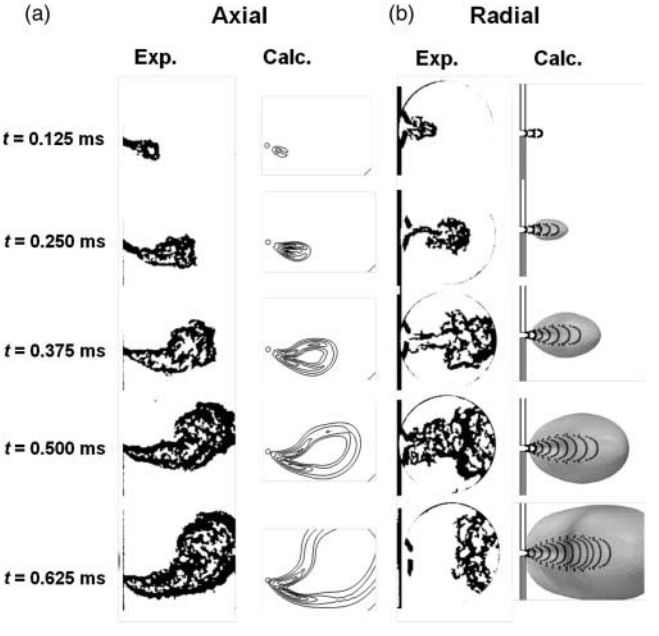

Figure 16. Comparison between experimental Schlieren images and computed contours of density gradient magnitude [21]. (a) Axial view. (b) Radial view with computed contours of progress variable taken at $c = 0.5$, location of channel particles represented with black points. Engine speed: 1250 rpm, lambda 1.0, peripheral ignition.

and computed time taken by the flame kernel to reach the volume of 0.1 cm^3 at constant engine speed, 1250 rpm, for both spark locations, as a function of the air-index excess. Generally, the two trends are in rather good agreement, with an overestimation of the required time for leaner conditions with peripheral ignition. However, since these conditions mainly differ because of the variation of the laminar flame speed with the air–fuel ratio, it is difficult to explain the observed divergent trend in the measured data from $\lambda = 1.3$ to $\lambda = 1.5$ between the central and peripheral ignition data.

Finally, Figures 15 and 16 show a qualitative comparison between the predicted flame development and Schlieren images for the peripheral spark location at stoichiometric conditions for different times from 0.125 to 0.625 ms. The three sequences evidence a rather good similarity among experimental and computational images, the effect of convection and turbulence on the flame kernel growth and development at 1250 rpm being evident, while these contributions are clearly low at 300 rpm and the flameholder behaviour of the spark plug.

5. Conclusions

A Lagrangian flame–kernel model to predict ignition in spark-ignition engine was presented and evaluated. The model takes into account all the physical and geometric parameters that influence the process of formation and development of the flame kernel: electrical circuit characteristic and heat transfer modes to the gas, local mixture and flow-field conditions, transition to a fully developed flame, geometrical characteristic of the spark and of the combustion chamber.

The proposed model has been preliminarily evaluated with experiments from Maly and Herweg [16] who investigated the flame kernel formation in a cylindrical transparent side engine chamber. Comparisons with experimental data evidenced a discrete capability of predicting the effects of variations of engine speed, air–fuel ratio and spark-plug position. Validation was performed by comparing computed and experimental evolution of the burnt gas volume. Comparisons with experimental data show that the proposed comprehensive approach is able to properly describe effects of local flow and air–fuel ratio on the flame kernel growth process. Further validation is necessary to understand the capability of the model to predict combustion under a wider range of operating conditions and in more realistic configurations.

References

[1] R. Borghi, *On the structure and morphology of turbulent premixed flames*, in *Recent Advances in the Aerospace Sciences*, C. Bruno and C. Casci, eds., Pergamon Press, London, 1984, pp. 117–138.

[2] O. Colin, A. Benkenida, and C. Angelberger, *3d modeling of mixing, ignition and combustion phenomena in highly stratified gasoline engines*, Oil Gas Sci. Technol. 58 (2003), pp. 47–62.

[3] F. Contino, H. Jeanmart, T. Lucchini, and G. D'Errico, *Coupling of in situ adaptive tabulation and dynamic adaptive chemistry: An effective method for solving combustion in engine simulations*, Proc. Combus. Inst. 33(2) (2011), pp. 3057–3064.

[4] A. D'Angola, G. Colonna, C. Gorse, and M. Capitelli, *Thermodynamic and transport properties in equilibrium air plasmas in a wide pressure and temperature range*, Eur. Phys. J. D 46 (2008), pp. 129–150.

[5] R. Dahms, T.D. Fansler, M.C. Drake, T.-W. Kuo, A.M. Lippert, and N. Peters, *Modeling ignition phenomena in spray-guided spark-ignited engines*, Proc. Combus. Inst. 32(2) (2009), pp. 2743–2750.

[6] R.N. Dahms, M.C. Drake, T.D. Fansler, T.-W. Kuo, and N. Peters, *Understanding ignition processes in spray-guided gasoline engines using high-speed imaging and the extended spark-ignition model SparkCIMM. Part A: Spark channel processes and the turbulent flame front propagation*, Combus. Flame 158(11) (2011), pp. 2229–2244.

[7] G. D'Errico, T. Lucchini, S. Merola, and C. Tornatore, *Application of a thermodynamic model with a complex chemistry to a cycle resolved knock prediction on a spark ignition optical engine*, Int. J. Auto. Technol. 13(3) (2012), pp. 389–399.

[8] J.M. Duclos and O. Colin, *Arc and kernel tracking ignition model for 3D spark-ignition engine calculations*, Proceedings of COMODIA 2001 Conference, Nagoja, 2001.

[9] J.P. Duclos, M. Zolver, and T. Baritaud, *3d modeling of combustion for Di-Si engines*, Oil Gas Sci. Technol. 54 (1999), pp. 259–264.
[10] S. Falfari and G. Bianchi, *Development of an ignition model for S.I. engines simulation*, SAE Paper, 2007-01-0148, 2007.
[11] R. Herweg, Ph. Begleris, A. Zettlitz, and G.F.W. Ziegler, *Flow field effects on flame kernel formation in a spark-ignition engine*, SAE Paper, 881639, 1988.
[12] J.B. Heywood, *Internal Combustion Engine Fundamentals*, McGraw-Hill, New York, 1988.
[13] J. Kim and K. Anderson, *Spark anemometry of bulk gas velocity at the plug gap of a firing engine*, SAE Paper, 952459, 1995.
[14] T. Lucchini, G. D'Errico, and D. Ettorre, *Numerical investigation of the spray-mesh-turbulence interactions for high-pressure, evaporating sprays at engine conditions*, Int. J. Heat Fluid Flow 32 (2011), pp. 285–297.
[15] T. Lucchini, G. D'Errico, A. Onorati, G. Bonandrini, L. Venturoli, and R. Di Gioia, *Development of a CFD approach to model fuel–air mixing in gasoline direct-injection engines*, SAE Paper, 2012-01-0146, 2012.
[16] R.R. Maly and R. Herweg, *A fundamental model for flame kernel formation in SI engines*, SAE Paper, 922243, 1992.
[17] A. Montanaro, L. Allocca, D. Ettorre, T. Lucchini, F. Brusiani, and G. Cazzoli, *Experimental characterization of high-pressure impinging sprays for CFD modeling of GDI engines*, SAE Int. J. Engines 4 (2011), pp. 747–763.
[18] N. Nordin, *Complex chemistry modeling of diesel spray combustion*, PhD thesis, Department of Thermo Fluid Dynamics, Chalmers University of Technology, 2001.
[19] OpenFOAM website. ESI Group, 2012. Available at http://www.openfoam.org.
[20] Yu.P. Raizer, *Gas Discharge Physics*, Springer, Berlin, 1991.
[21] G.S. Settles, *Schlieren and Shadowgraph Techniques*, Springer, Berlin, 2001.
[22] H. Shen, P. Hinze, and J. Heywood, *A model for flame initiation and early development in SI engine and its application to cycle-to-cycle variations*, SAE Paper, 942049, 1994.
[23] J. Song and M. Sunwoo, *A modeling and experimental study of initial flame kernel development and propagation in SI engines*, SAE Paper, 2000-01-0960, 2000.
[24] Z. Tan and R.D. Reitz, *Modeling ignition and combustion in spark-ignition engines using a level-set method*, SAE Paper, 2003-01-0722, 2003.
[25] M. Thiele, S. Selle, U. Riedel, J. Warnatz, and U. Maas, *Numerical simulation of spark ignition including ionization*, Proc. Combus. Inst. 28 (2000), pp. 1177–1185.
[26] H. Willems and R. Sierens, *Modeling the initial growth of the plasma and flame kernel in SI engines*, J. Eng. Gas Turbines Power 125 (2003), pp. 479–484.
[27] X. Yang, A. Solomon, and T. Kuo, *Ignition and combustion simulations of spray-guided SIDI engine using Arrhenius combustion with spark-energy deposition model*, SAE Paper, 2012-01-0147, 2012.
[28] K. Yun, S. Lee, and N. Sung, *A study of the propagation of turbulent premixed flame using the flame surface density model in a constant volume combustion chamber*, KSME Int. J. 16(4) (2002), pp. 564–571.